Research Article | Open Access

Microstructures

Lu et al. Microstructures 2026, 6, 20260135 DOI:10.20517/microstructures.2026.93

Incommensurate modulations and thickness-dependent energy storage density in (PbLaSrBa)(ZrSnTi)O_3 relaxor antiferroelectric thick-film ceramics

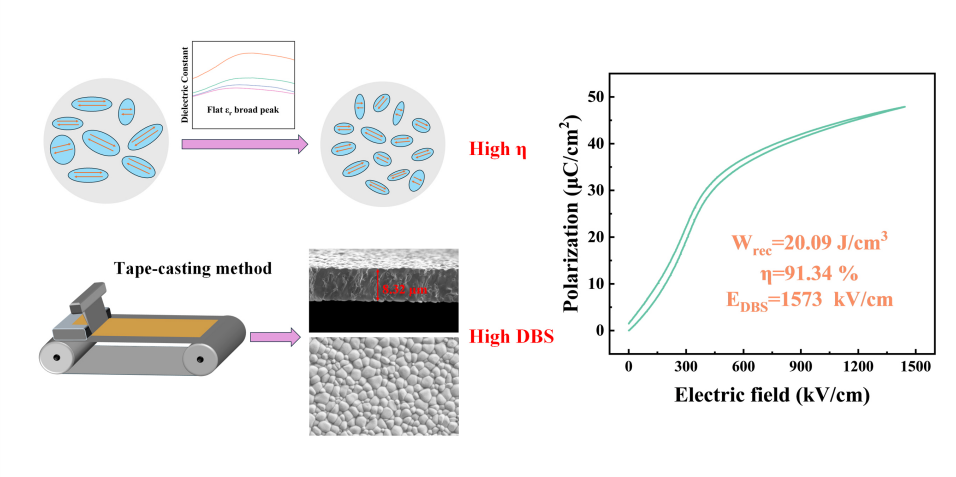
Sheng-Guo Lu[1], Xuling Yan[1], Xiaoyi Gao[2], Chao Yu[1], Yuxuan Li[1], Shibin Wang[1], Yingbang Yao[1], Tao Tao[1], Bo Liang[1], Weiping Gong[3], Xiang Niu[1], Xiaodong Jian[1,4]

Keywords:
(PbLaSrBa)(ZrSnTi)O_3, antiferroelectrics, thick-film ceramics, energy storage performance, energy storage density versus thickness

Citation: Lu, S. G.; Yan, X.; Gao, X.; Yu, C.; Li, Y.; Wang, S.; Yao, Y.; Tao, T.; Liang, B.; Gong, W.; Niu, X.; Jian, X. Incommensurate modulations and thickness-dependent energy storage density in (PbLaSrBa)(ZrSnTi)O_3 relaxor antiferroelectric thick-film ceramics. *Microstructures* **2026**, *6*, 20260135. https://dx.doi.org/10.20517/microstructures.2026.93

Received: 4 May 2026
First Decision: 2 Jun 2026
Revised: 14 Aug 2026
Accepted: 26 Aug 2026
Published: 28 Oct 2026

Academic Editor: Dae-Yong Jeong
Copy Editor: Ping Zhang
Production Editor: Ping Zhang



Abstract

In this study, $(Pb_{0.92-x}La_{0.04}Sr_xBa_{0.02})(Zr_{0.64}Sn_{0.35}Ti_{0.01})O_3$ (PLSBZSTi, i = 1 (x=0.04), 2 (0.06), 3 (0.08), and 4 (0.10)) relaxor antiferroelectric thick-film ceramics were prepared using a tape-casting process. An ultrahigh W_{rec} of 20.09 J/cm³ with an ultrahigh η of 91.34% was obtained for the PLSBZST2 (x = 0.06) ceramic. This outstanding energy storage performance is attributed to the distinct microstructural features of this system. Specifically, transmission electron microscopy revealed the presence of nanosized stripe domains, along with F-spots associated with 1/2{ooo} superlattice diffraction and an incommensurate modulation structure (IMS) related to the 1/n<110> superlattice (n = 4.91). These microstructural characteristics are direct evidence of oxygen octahedral tilting, which promotes the formation of relatively slim hysteresis loops. Moreover, the inverse power-law relationship between the sample thickness and energy storage density was determined. The fitted exponent was -0.43 ± 0.04, which can be quantified by combining the thickness-dependent dielectric breakdown strength (exponent of -0.39) and

[1]State Key Laboratory of Precision Electronic Manufacturing Technology and Equipment, Guangdong Provincial Research Center on Smart Materials and Energy Conversion Devices, School of Materials and Energy, School of Electromechanical Engineering and School of Integrated Circuits, Guangdong University of Technology, Guangzhou 510006, Guangdong, China.
[2]Shandong Provincial Key Laboratory of High-Performance Ceramics and Precision Manufacturing, Shandong Industrial Ceramics Research and Design Institute Co., Ltd, Zibo 255000, Shandong, China.
[3]Guangdong Provincial Key Laboratory of Electronic Functional Materials and Devices, Huizhou University, Huizhou 516001, Guangdong, China.
[4]Science and Technology on Reliability Physics and Application of Electronic Component Laboratory, The 5th Electronics Research

Institute of the Ministry of Industry and Information Technology, Guangzhou 510610, Guangdong, China.

Correspondence to: Prof. Sheng-Guo Lu, Dr. Shibin Wang, Dr. Xiang Niu, State Key Laboratory of Precision Electronic Manufacturing Technology and Equipment, Guangdong Provincial Research Center on Smart Materials and Energy Conversion Devices, School of Materials and Energy, School of Electromechanical Engineering and School of Integrated Circuits, Guangdong University of Technology, Guangzhou 510006, Guangdong, China. E-mail: sglu@gdut.edu.cn; shibinwang@gdut.edu.cn; Xiang.Niu@gdut.edu.cn; Dr. Xiaoyi Gao, Shandong Provincial Key Laboratory of High-Performance Ceramics and Precision Manufacturing, Shandong Industrial Ceramics Research and Design Institute Co., Ltd, Zibo 255000, Shandong, China. E-mail: xygao@whut.edu.cn; Dr. Xiaodong Jian, State Key Laboratory of Precision Electronic Manufacturing Technology and Equipment, Guangdong Provincial Research Center on Smart Materials and Energy Conversion Devices, School of Materials and Energy, School of Electromechanical Engineering and School of Integrated Circuits, Guangdong University of Technology, Guangzhou 510006, Guangdong, China; Science and Technology on Reliability Physics and Application of Electronic Component Laboratory, The 5th Electronics Research Institute of the Ministry of Industry and Information Technology, Guangzhou 510610, Guangdong, China. E-mail: jianxiaodong_gdut@126.com

maximum polarization (exponent of -0.13) with a 20% correction factor accounting for the practical underutilization of the maximum electric field and polarization.

INTRODUCTION

Compared with traditional lithium-ion batteries, electrochemical capacitors, and polymer media, ceramic-based dielectric capacitors offer high power densities and are attractive for meeting the growing demand for energy storage devices[1-5], and many studies have attempted to develop these systems[6-10]. Ceramic-based dielectric capacitors have attracted much attention because of their high power densities, fast charge-discharge abilities, broad operating-temperature ranges, long cyclic times, and excellent thermal stabilities in pulse-power devices[11-16]. These characteristics make ceramic dielectric capacitors promising for energy storage applications such as pulse-power supplies, electric vehicles, and electromagnetic pulse devices[17-19].

Dielectric materials can be classified into four categories: linear dielectrics, normal ferroelectrics, antiferroelectrics (AFEs), and relaxor ferroelectrics[20-23]. Among them, AFEs show unique double polarization-electric field (P-E) hysteresis loops in an external electric field, experience a transition from an AFE phase to a ferroelectric (FE) phase with an increasing electric field, and demonstrate a transition from an FE to AFE phase in a decreasing electric field. Because of the antiparallel arrangement of adjacent dipoles, the remnant polarization of AFEs is near zero, and the polarization and dielectric constant sharply increase when the electric field reaches the transition field. These features improve the discharged energy storage density and charge-discharge performance of AFEs in terms of increasing the integrated area of the upper branch of P-E hysteresis loop with respect to the polarization axis[24-27]. The total energy storage density (W_{tot}), recoverable energy storage density (W_{rec}), and energy storage efficiency (η) of dielectric ceramic capacitors can be defined as follows[28,29]:

$$W_{tot} = \int_0^{P_m} E dP \tag{1}$$

$$W_{rec} = \int_{P_r}^{P_m} E dP \tag{2}$$

$$\eta = \frac{W_{rec}}{W_{tot}} \times 100\% \tag{3}$$

where E, P_m, and P_r denote the applied electric field, maximum polarization, and remnant polarization, respectively.

Therefore, improving the polarization, AFE-FE transition field, and dielectric breakdown strength (DBS) of AFE materials can enhance the energy storage performance of dielectric capacitors. The stability of the AFE phase can be evaluated using the Goldschmidt tolerance factor for the ABO_3 perovskite structure:

$$t = \frac{R_A + R_O}{\sqrt{2}\,(R_B + R_O)} \tag{4}$$

where R_A, R_B, and R_O denote the radii of A-site, B-site, and oxygen ions, respectively. When ionic doping decreases t, the stability of the AFE phase increases, thus increasing the phase transition field $E_{AFE\text{-}FE}$. For linear ferroelectrics, the polarization is usually proportional to the dielectric constant multiplied by the electric field, and it therefore increases with increasing electric field intensity. The DBS can be increased either intrinsically by increasing the bandgap through doping or extrinsically by refining the grain-size distribution to reduce defect concentration and interfacial flaws[30-32]. Liu *et al.*[32,33] investigated $(Pb_{0.925}La_{0.05})(Zr_{0.995}Ti_{0.005})O_3$ ceramics and obtained W_{rec} = 12.3 J/cm³ and η = 84% under an electric field of 420 kV/cm by refining the grain size distribution and enhancing the bandgap ($E_B \propto e^{\sqrt{E_g}}$), where E_B is the DBS and E_g is the bandgap). Liu *et al.*[31] also prepared a multilayer ceramic capacitor $(Pb_{0.94}La_{0.02}Ca_{0.04})(Zr_{0.7}Sn_{0.3})_{0.995}O_3$ via grain refinement and strengthened cation-O bonding, obtaining W_{rec} = 14.3 J/cm³ and η = 86.1% at 530 kV/cm. In addition, Li *et al.*[34] investigated $(Pb_{0.92}Gd_{0.02}Sr_{0.05})(Zr_{0.87}Sn_{0.12}Ti_{0.01})O_3$ ceramics and achieved W_{rec} = 14.5 J/cm³ and η = 81% at 717 kV/cm using a phase tailoring strategy via chemical modification.

These previous studies found that although these materials demonstrate high energy-storage densities, their energy storage efficiencies remain relatively low. By contrast, the energy storage efficiency of $(PbLa)(ZrSnTi)O_3$ (PLZST) ceramics is related to the hysteresis of the AFE-FE and FE-AFE phase transitions. Previous investigations have shown that the electric hysteresis in the P-E loop can be reduced by doping Sr^{2+} ions at A-sites, and a relaxor AFE with a diffuse phase transition can be constructed to form a slim P-E hysteresis loop, thereby effectively improving the energy storage efficiency of this system[11,35]. Moreover, the doping of Ba^{2+} ions at A-sites has been shown to increase the dielectric constant and correspondingly decrease the phase transition temperature[36,37]. Therefore, this study investigated Ba^{2+} and Sr^{2+} co-doped PLZST AFE bulk ceramics. In addition, doped PLZST thick-film ceramics were fabricated using a tape-casting process to further improve the DBS and energy storage performance[38]. The effect of film thickness on DBS and polarization was evaluated, and the influence of the ceramic thickness on the energy storage density was statistically determined.

EXPERIMENTAL

Experimental methods

First, $(Pb_{0.92-x}La_{0.04}Sr_xBa_{0.02})(Zr_{0.64}Sn_{0.35}Ti_{0.01})O_3$ (where x = 0.04, 0.06, 0.08, and 0.10; abbreviated as PLSBZST1, PLSBZST2, PLSBZST3, and PLSBZST4, respectively) ceramics were prepared using a tape-casting approach. Raw materials were purchased from Aladdin (China), including PbO (99.90%), La_2O_3 (99.90%), $SrCO_3$ (99.00%), $BaCO_3$ (99.95%), ZrO_2 (99.99%), SnO_2 (99.50%), and TiO_2 (99.00%). The raw materials were weighed according to their stoichiometric ratios, and an excess of 3% PbO was added to compensate for PbO volatilization during high-temperature sintering. The mixture was ball milled (MSK-SFM-1, Kejing, China) at 250 rpm for 24 h using anhydrous ethanol as a solvent, dried at 100 °C overnight after ball milling, and the resulting green powders were calcined at 900 °C for 2 h. A second ball milling and drying step was then performed to obtain crystalline PLSBZST powders. Next, the PLSBZST ceramic powders were dispersed in a solvent. The dispersant, binder, and plasticizer were then added to prepare the slurry, which was tape-cast into PLSBZST thick-film green sheets. Finally, the thick-film green sheets were cut and debindered at 650 °C for 6 h, followed by sintering at 1,100~1,200 °C for 6 h to obtain dense, freestanding thick-film ceramics.

Microstructural characterization and performance testing

The lattice structure was characterized using X-ray diffractometry (XRD; Rigaku, Ultima-Ⅳ). Rietveld refinement was carried out using FullProf software. The surface morphologies and elemental distributions of the ceramics were analyzed using scanning electron microscopy (SEM; S3400-N and SU8010, Hitachi

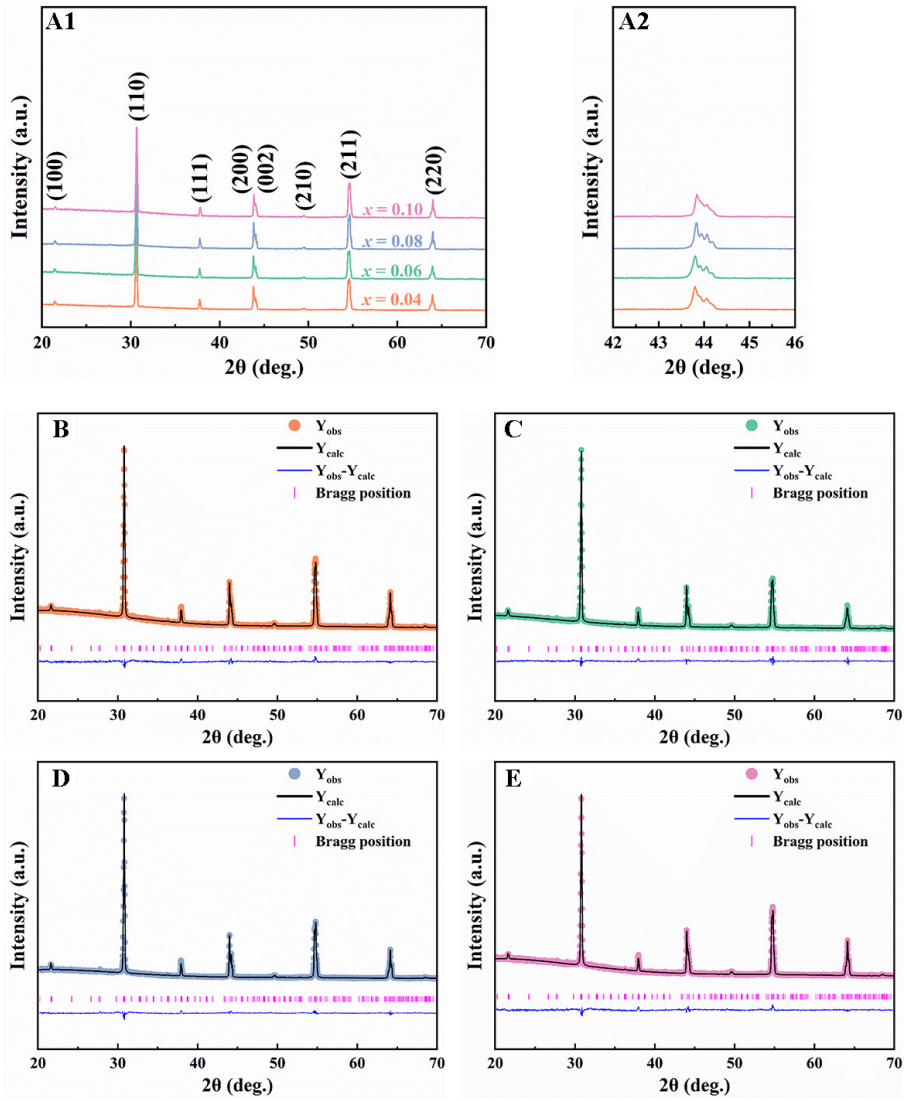


Figure 1. (A1) XRD patterns obtained at room temperature for the PLSBZST thick-film ceramics; (A2) Magnified XRD patterns for 2θ ranging from 42° to 46°; and Rietveld refinements for $(Pb_{0.92-x}La_{0.04}Sr_xBa_{0.02})(Zr_{0.64}Sn_{0.35}Ti_{0.01})O_3$ thick-film ceramics with different x values: (B) x = 0.04, (C) x = 0.06, (D) x = 0.08, (E) x = 0.10. XRD: X-ray diffraction; PLSBZST: $(Pb_{0.92-x}La_{0.04}Sr_xBa_{0.02})(Zr_{0.64}Sn_{0.35}Ti_{0.01})O_3$.

High-Technologies Corporation, Japan) equipped with an energy-dispersive X-ray spectrometer (EDS). The grain size distribution was statistically analyzed using ImageJ software. Selected-area electron diffraction (SAED) patterns and high-resolution transmission electron microscopy (HRTEM) images were obtained using a Talos F200x microscope (FEI Company, USA). The temperature- and frequency-dependent dielectric constant and loss tangent were measured using a precision inductor-capacitor-resistor (LCR) analyzer (4980A, Keysight, USA). The P-E hysteresis loops of the ceramics were measured using a Sawyer-Tower circuit (Precision Multiferroic II ferroelectric test system, Radiant Technologies Inc., USA). Circular gold electrodes with a diameter of 1 mm were used for the P-E and other electrical measurements, whereas electrodes with a diameter of 1.8 mm were used for the charge-discharge measurements.

RESULTS AND DISCUSSION

Figure 1A shows the XRD patterns of the PLSBZST1-4 AFE ceramics at room temperature. All ceramics demonstrate pure perovskite structures, and no diffraction peaks from the impurity phase are detected. In the magnified patterns near $2\theta = 44°$, the intensity of the (200) peak is approximately twice that of the (002) peak, indicating that the PLSBZST ceramics may have an orthorhombic structure[30,39,40]. According to the Bragg equation,

Table 1. Lattice parameters obtained using Rietveld refinement

Composition	Lattice parameters				Phase	R_p (%)	R_{wp} (%)	χ^2
	a (Å)	b (Å)	c (Å)	A = β = γ (°)				
x = 0.04	5.82617	11.63645	8.18836	90	O	4.03	5.32	2.44
x = 0.06	5.82586	11.63240	8.18749	90	O	3.65	4.87	2.37
x = 0.08	5.82329	11.62583	8.18616	90	O	4.02	5.25	2.04
x = 0.10	5.82280	11.62437	8.18529	90	O	3.70	4.74	2.94

R_p: Patterns; R_{wp}: weighted patterns.

$$2dsin\theta = n\lambda \tag{5}$$

where d is the distance between the two close crystalline planes, θ is the angle of incidence or the angle of reflection, n is the whole number, and λ is the wavelength of X-ray. The lattice shrinks and the lattice constant decreases as Sr^{2+} (1.19 Å) has a smaller ionic radius than Pb^{2+} (1.49 Å). Therefore, the diffraction peaks shift toward higher diffraction angles.

Rietveld refinements were used to confirm the exact phase structures and detailed lattice parameters of all samples. Figure 1B-E demonstrates the Rietveld refinement results of the PLSBZST thick-film ceramics, which show that all thick-film ceramics adopt an orthorhombic phase structure (*Pbam* space group). Table 1 summarizes the lattice parameters and reasonable agreement indices (R_p, R_{wp}, and χ^2).

To further characterize the microstructures of PLSBZST ceramics, the sample with x = 0.06 was analyzed using transmission electron microscopy (TEM). In Figure 2A, typical nanosized stripe electric domains (e.g., ~200-300 nm in size) can be observed in the bright-field image. An HRTEM image covering an electric domain area with tens of nanometers in size is also shown in the inset of Figure 2A. The reduction in the size of the ordered regions is attributed to the disruption of long-range order caused by compositional and structural fluctuations. These nanosized domains, also called polar nanoregions (PNRs), result in slim P-E hysteresis loops and other typical relaxor AFE behaviors, such as diffuse phase transitions[11,35]. Moreover, the relaxor AFE diffuseness parameter is > 1 and close to 1.6 (see Figure 2A)[41,42]. Figure 2B shows the SAED pattern obtained along the $[0\bar{1}1]$ zone axis. In addition to the main reflection spots, 1/2{ooo}-type superlattice diffraction patterns (F-spots) are observed and indicated by the red boxes in Figure 2B. These reflections arise from the tilting of the oxygen octahedra within the crystalline structure. In Figure 2C and 2D, the diffraction spots indicated by the hollow triangles are adjacent to the main diffraction spots, which may result from the incommensurate modulation structure (IMS) caused by the antiparallel displacement of cations[43,44]. As shown in Figure 2C, the IMS is formed along the $<\bar{1}0\bar{1}>$ direction. The plane spacing ($d_{10\bar{1}}$) results from an irrational number multiplied by the modulation wavelength in the diffraction spacing (λ) (i.e., $d_{10\bar{1}} = n\lambda$, where $n = 4.91$)[43]. Figure 2D shows the SAED patterns obtained in the [010] direction near the 90° domain wall. The satellite patterns caused by the IMS are highlighted by the green and yellow hollow triangles, and these reflection patterns are arranged vertically along the <101> and $<\bar{1}01>$ directions[44]. The existence of the IMS can produce a relatively slimmer hysteresis loop. For the relaxor AFE with an IMS structure, the shape of the hysteresis loop is slimmer and more inclined, which improves the energy storage density and efficiency of this system.

Figure 3A-D presents the surface SEM images of the four PLSBZST thick-film ceramics and their grain size distributions. All ceramic samples show dense microstructures, clear grain boundaries, closely packed grains, and small pores at multigrain junctions. The inset of each panel shows the grain size distribution histogram obtained using ImageJ software. The grain sizes are mainly distributed between 1 and 3 μm. These fine grain

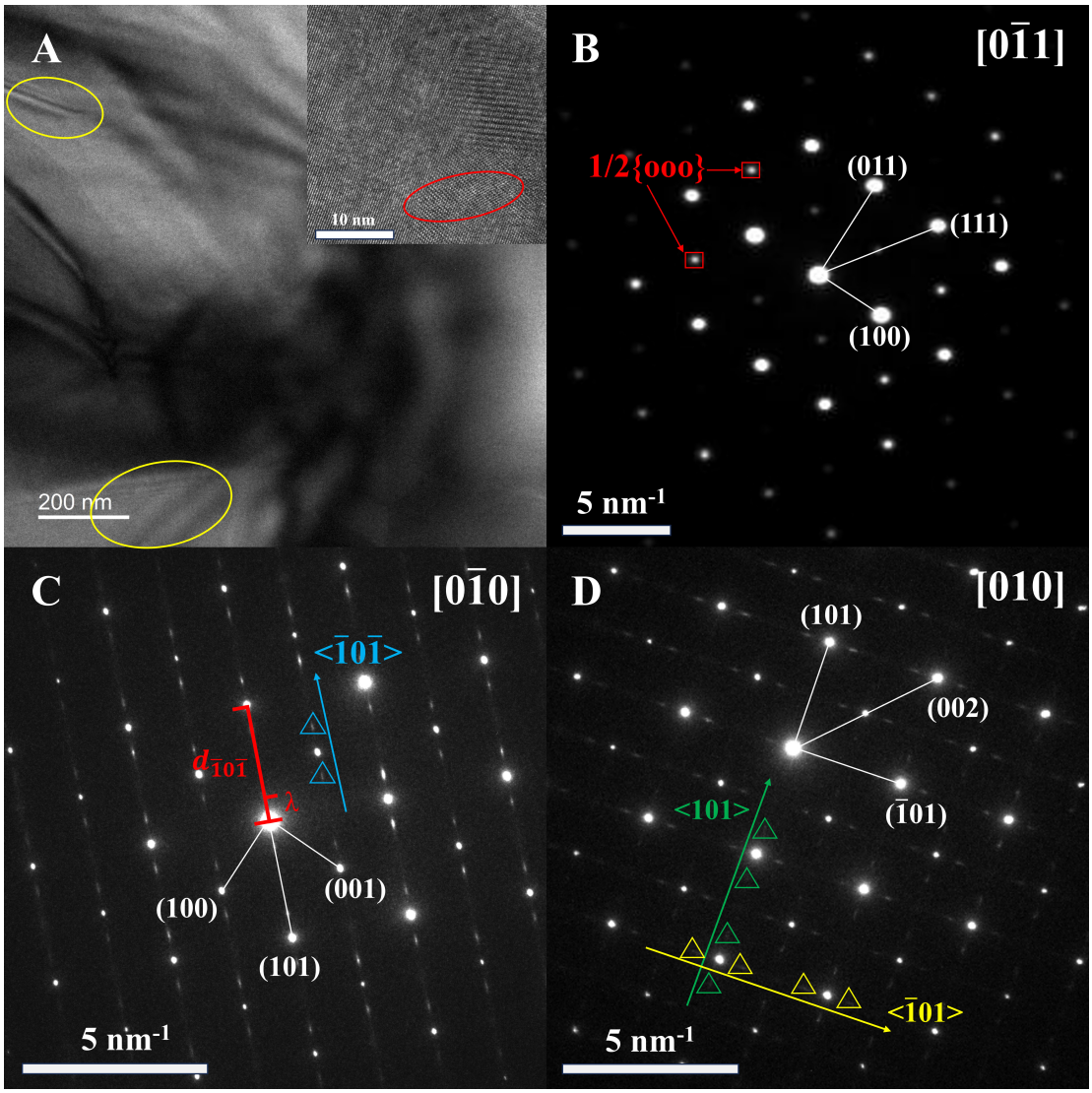


Figure 2. TEM image and diffraction patterns for PLSBZST2 (x = 0.06) AFE thick-film ceramics. (A) Bright-field images of the stripe domains, and the inset shows an HRTEM image of a nanosized domain; (B) SAED pattern with 1/2{ooo} superlattice patterns (F-spots); (C) [0 $\bar{1}$ 0] SAED pattern showing the incommensurate modulation structure (IMS) in an AFE domain; (D) [010] SAED pattern demonstrating the IMS near the 90° domain wall. TEM: Transmission electron microscopy; AFE: antiferroelectric; PLSBZST2: $(Pb_{0.86}La_{0.04}Sr_{0.06}Ba_{0.02})(Zr_{0.64}Sn_{0.35}Ti_{0.01})O_3$; SAED: selected area electron diffraction; HRTEM: high resolution transmission electron microscopy.

sizes improve the DBS of the ceramics via the relation $E_B \propto G^{-a}$, where E_B is the DBS, G is the average grain size, and a is a constant[45]. As shown in Figure 3E, the cross-sectional SEM image indicates that the thickness of the PLSBZST1 thick-film ceramic is 8.32 ± 0.67 μm, and the thicknesses of the other three samples (PLSBZST2, PLSBZST3, and PLSBZST4) are 7.00 ± 0.20, 7.26 ± 0.07, and 8.59 ± 0.15 μm, respectively. The distribution of elements is another important factor affecting the DBS of the dielectric ceramics. An uneven elemental distribution can lead to local dielectric breakdown and eventually failure of the entire ceramic, which is not conducive to improving energy storage performance[46]. Figure 3F shows the surface morphology and EDS mappings of all elements in the PLSBZST1 thick-film ceramic in the selected area (inside the red box). The elemental maps show that Pb, La, Sr, Ba, Zr, Sn, Ti, and O are evenly distributed throughout the analyzed area, with no obvious elemental aggregation observed, which helps enhance the energy storage performance of these ceramics.

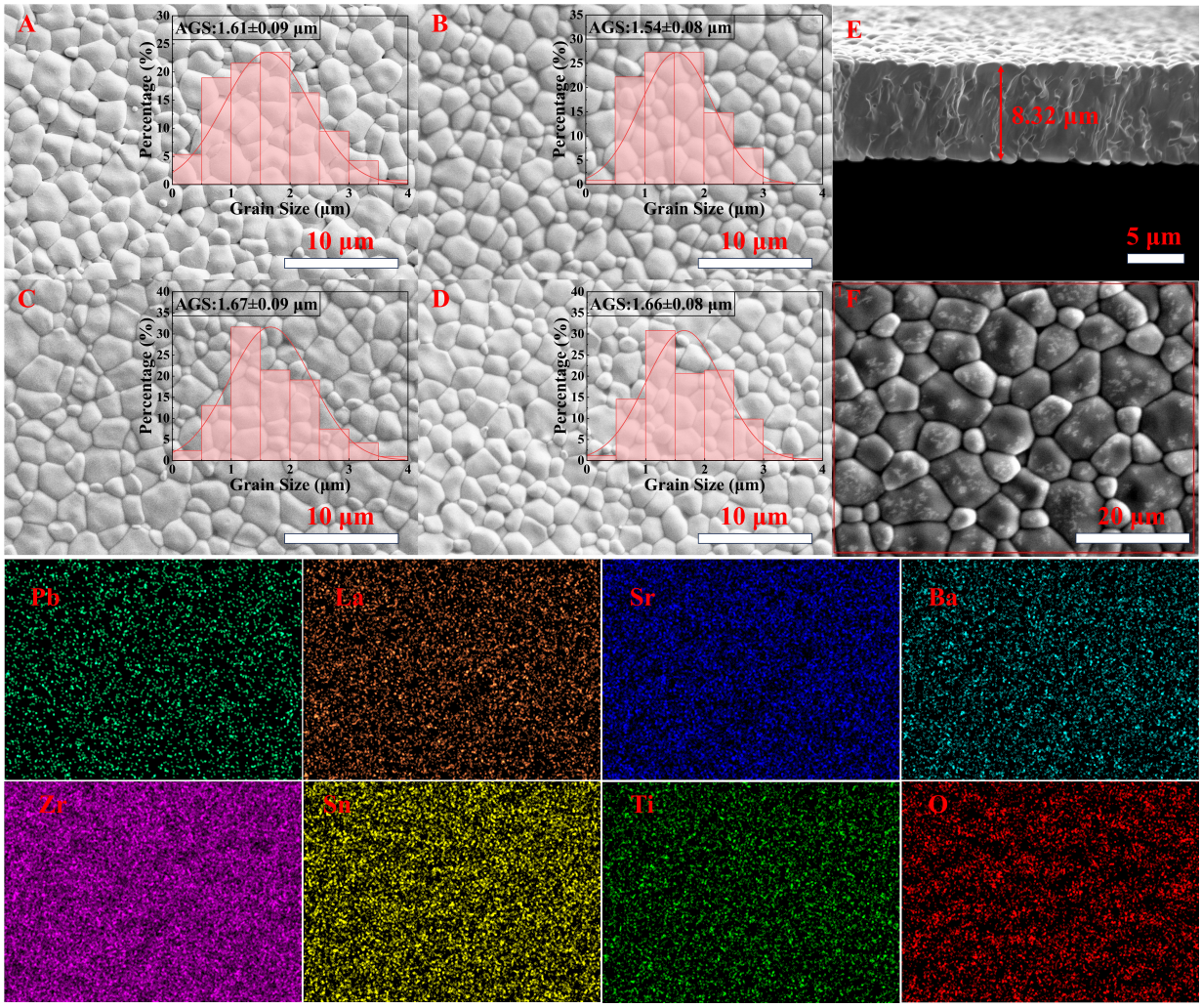


Figure 3. (A-D) SEM images of the PLSBZST thick-film ceramics; (E) Cross-sectional SEM image of the PLSBZST1 sample; (F) Surface morphology and SEM-EDS elemental mappings (Pb, La, Sr, Ba, Zr, Sn, Ti, O) of the PLSBZST1 sample; the scale bar for these mappings is shown in (F). SEM: Scanning electron microscopy; PLSBZST: $(Pb_{0.92-x}La_{0.04}Sr_xBa_{0.02})(Zr_{0.64}Sn_{0.35}Ti_{0.01})O_3$; EDS: energy-dispersive X-ray spectrometer.

Figure 4A-D shows the temperature-dependent relative dielectric constant (ε_r) and loss tangent (tanθ) for PLSBZST ceramics at frequencies of 1, 5, 10, and 50 kHz in the temperature range of 30-320 °C. At a constant temperature, the slight decrease in the dielectric constant with increasing measurement frequency is attributed to the reduced ability of dipoles to follow the alternating field at high frequencies[43]. The maximum dielectric constant (ε_m) gradually decreases with increasing Sr^{2+} content, and the peak temperature (T_m) corresponding to ε_m also decreases. Due to the influence of the thermodynamic instability of $PbSnO_3$, all the samples underwent a stage in which the dielectric constant showed little variation and resulted in a flat, broad peak. This behavior is attributed to the occurrence of a multicell cubic (MCC) phase[47], which exhibits dielectric characteristics similar to those of the relaxor AFEs. To further examine the relaxor AFE characteristics of PLSBZST thick-film ceramics, the modified Curie-Weiss law was used[33]

$$\frac{1}{\varepsilon_r} - \frac{1}{\varepsilon_m} = \frac{(T - T_m)^\gamma}{c} \tag{6}$$

where T is the temperature above T_m, ε_r is the relative dielectric constant at T, ε_m is the maximum dielectric constant, C is the Curie constant, and γ is the diffuseness parameter. As shown in Figure 4E, γ increases with

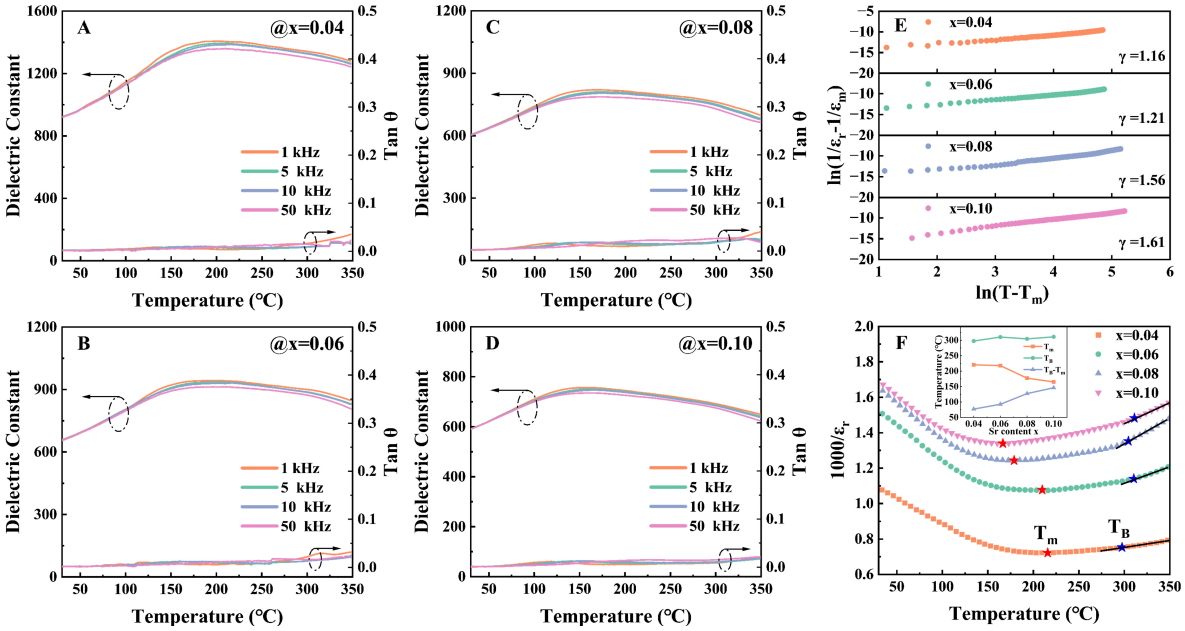


Figure 4. (A-D) Dielectric constant and loss tangent as a function of temperature for PLSBZST thick-film ceramics at 1, 5, 10, and 50 kHz; (E) $\ln(1/\varepsilon_r\text{-}1/\varepsilon_m)$ as a function of $\ln(T\text{-}T_m)$ at 10 kHz. (F) Inverse dielectric constant ($1000/\varepsilon_r$) as a function of temperature at 10 kHz; the inset shows T_m, T_B, and T_B-T_m as a function of the Sr^{2+} content. Moreover, the red stars denote T_m, while the blue stars denote T_B. PLSBZST: $(Pb_{0.92-x}La_{0.04}Sr_xBa_{0.02})(Zr_{0.64}Sn_{0.35}Ti_{0.01})O_3$.

increasing x from 1.16 (x = 0.04) to 1.61 (x = 0.10). This indicates that the relaxor AFE characteristics of PLSBZST thick-film ceramics are gradually enhanced under these conditions.

In Figure 4F, $1000/\varepsilon_r$ as a function of temperature, based on the dielectric constant versus temperature plot, clearly shows the degree of diffuseness. T_B is the Burns temperature, defined as the formation of polar nano regions in relaxor ferroelectrics, at which ε_r begins to deviate from the Curie-Weiss law. The results show that T_B-T_m and the degree of diffuseness increase with increasing Sr^{2+} content. The increase in the diffuse degree and relaxor AFE character is beneficial for refining the P-E hysteresis loop, thus obtaining higher W_{rec} and η values[31,32,48,49].

Figure 5A and B shows the P-E and current - electric field (I-E) hysteresis loops for the PLSBZST1-4 thick-film ceramics at room temperature. All PLSBZST ceramic samples show typical AFE hysteresis loops and bimodal current curves. With increasing Sr^{2+} content, the P-E hysteresis loop exhibits stronger relaxor AFE characteristics, the I-E current peaks broaden, and the peaks shift towards high electric fields, which indicates that the AFE-FE phase transition electric field increases with x[11].

The AFE-FE and FE-AFE phase transition electric fields and hysteresis width for the four ceramics ($\Delta E = E_{AFE\text{-}FE} - E_{FE\text{-}AFE}$) are shown in Figure 5C. It can be seen that $E_{AFE\text{-}FE}$ and $E_{FE\text{-}AFE}$ increase from 306.08 and 260.45 kV/cm for PLSBZST1 to 328.68 kV/cm and 287.99 kV/cm for PLSBZST4, and ΔE decreases from 45.63 kV/cm for x = 0.04 to 34.59 kV/cm for x = 0.06, then increases with increasing x (x = 0.08, 0.10). Doping the A sites with elements of smaller ionic radii enhances the stability of the AFE phase and increases the AFE-FE transition field[38]. The increase in $E_{AFE\text{-}FE}$ and $E_{FE\text{-}AFE}$ increases the area between the up branch of the P-E loop and the polarization axis, thus increasing the discharged energy density W_{rec}. A decrease in ΔE results in a higher energy storage efficiency η. As shown in Figure 5C, the maximum polarization (P_{max}) gradually decreases with increasing Sr^{2+} content. On the one hand, the decrease in P_{max} results from the Pb^{2+} ions being replaced by Sr^{2+} ions with smaller ionic radii, which leads to the shrinking of the unit cells and

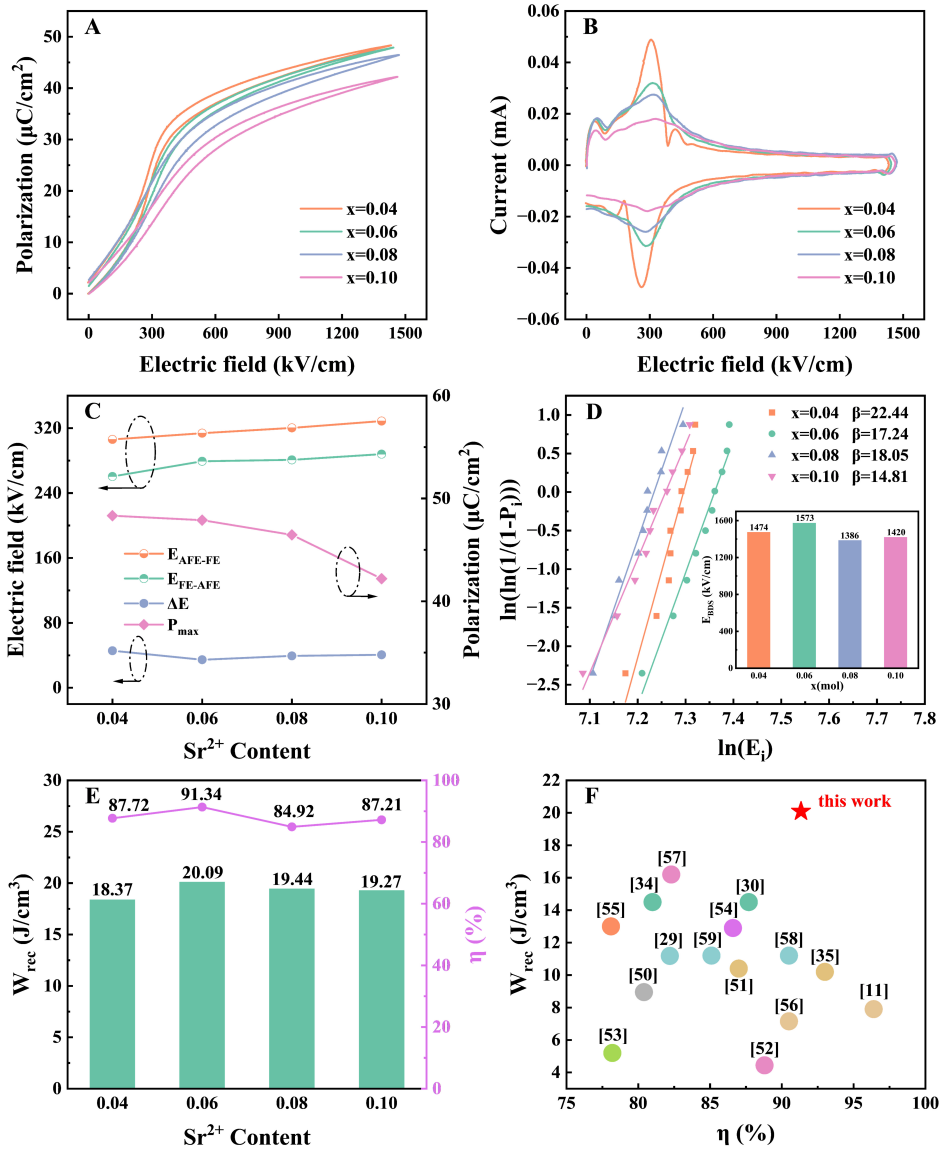


Figure 5. (A) P-E and (B) current - electric field (I-E) hysteresis loops obtained at room temperature for PLSBZST thick-film ceramics; (C) E_{AFE-FE}, E_{FE-AFE}, ΔE, and P_{max}; (D) Weibull distribution of the four samples, with the inset showing the DBS as a function of x; (E) W_{rec} and η for four samples; (F) Comparison of the W_{rec} and η values of PLSBZST2 with those of recently reported AFE ceramics[11,29,30,34,35,50-59]. P-E: Polarization - electric field; PLSBZST: $(Pb_{0.92-x}La_{0.04}Sr_xBa_{0.02})(Zr_{0.64}Sn_{0.35}Ti_{0.01})O_3$; DBS: dielectric breakdown strength; AFE: antiferroelectric; P_{max}: maximum polarization; W_{rec}: recoverable energy storage density.

hinders the relative displacement and movement space of the ions at the A sites, thereby decreasing the polarization[35]. This also affects the AFE-FE phase transition. With increasing Sr^{2+} content, the stability of AFE and the interaction between the two adjacent antiparallel dipoles in the AFE domain increase. Consequently, dipole switching within the AFE unit cells becomes more difficult, fewer dipoles align with the electric field, and the AFE-FE transition shifts to a higher electric field[50]. A similar phenomenon has also been reported for Sr^{2+}-doped $PbZrO_3$-based AFE ceramics[11,30].

Figure 5D shows the Weibull distribution results used to obtain the DBS. The slopes (βs) of all the Weibull distributions are > 14, indicating that all the specimens have better qualities (e.g., DBS, consistency, narrow distribution of the DBS, *etc.*). The Weibull distribution results show that the PLSBZST2 (x = 0.06) sample demonstrated the highest DBS among the four thick-film ceramics, and it was approximately 7.00 ± 0.20 μm

thick. These results indicate that a fine and uniform grain-size distribution, dense microstructure, and small ceramic thickness can effectively improve DBS.

The W_{rec} and η values for the PLSBZST ceramics are shown in Figure 5E to further investigate the energy storage performance of the PLSBZST ceramics. The PLSBZST2 (x = 0.06) ceramic sample demonstrates the highest W_{rec} and η values among all specimens, at 20.09 J/cm^3 and 91.34%, respectively. With increasing Sr^{2+} content, P_{max} gradually decreases. However, the W_{rec} values of the PLSBZST3 (x = 0.08) and PLSBZST4 (x = 0.10) ceramic samples are larger than those of PLSBZST1 (x = 0.04) due to the increase in the relaxor AFE characteristics. Finally, as shown in Figure 5F, the W_{rec} and η values for PLSBZST2 are compared with those recently published for AFE ceramics[11,29,30,34,35,50-59]. The enhanced W_{rec} and η will be favorable for the larger discharged energy density and higher energy efficiency of the pulse power capacitors.

The analysis of the P-E hysteresis loops indicated that the PLSBZST2 ceramic sample exhibits the highest W_{rec} among all PLSBZST AFE ceramics. In addition, the stability of W_{rec} with respect to temperature and frequency is an important parameter for evaluating the energy-storage performance of dielectric capacitors[60]. Figure 6A shows the P-E hysteresis loops of the PLSBZST2 ceramic at 940 kV/cm and 10 Hz over the temperature range of 30-110 °C. The E_{AFE-FE}, E_{FE-AFE}, ΔE, and P_{max} values as a function of temperature for PLSBZST2 ceramics are shown in Figure 6B. As temperature increases, the hysteresis loop slightly widens, which can be attributed to the continuous increase in the loss tangent. Moreover, P_{max} decreases almost linearly from 41.13 to 36.86 μC/cm^2 at 940 kV/cm with increasing temperature, which is probably due to the diffuse phase transition from an orthorhombic phase to a MCC phase[31], whereas ΔE increases from 14.87 to 39.89 kV/cm. The W_{rec} and η values as a function of temperature for the PLSBZST2 ceramics are shown in Figure 6C. With increasing temperature, W_{rec} gradually decreases from 13.39 to 11.65 J/cm^3, corresponding to a variation of less than 15%. By contrast, η is initially constant with increasing temperature and then slightly decreases but remains above 86%. Because temperature does not significantly affect the shape of the P-E hysteresis loop, W_{rec} and η values show very small variations with increasing temperature, demonstrating excellent temperature stability. Figure 6D shows the P-E hysteresis loops for the PLSBZST2 ceramics at 880 kV/cm and room temperature over the frequency range of 0.2-100 Hz. The corresponding E_{AFE-FE}, E_{FE-AFE}, ΔE, and P_{max} values are shown in Figure 6E as a function of frequency. With increasing measurement frequency, P_{max} slightly decreases from 40.8 to 39.60 μC/cm^2 at 880 kV/cm, corresponding to a variation of less than 3%, which is due to the small variation in the shape of the P-E hysteresis loop with increasing frequency. E_{AFE-FE} and ΔE monotonically increase with increasing frequency, and E_{FE-AFE} slightly decreases, resulting in a slowly increasing energy storage density and efficiency for PLSBZST2 [Figure 6F]. At a low frequency of 0.2 Hz, W_{tot} is the largest among the tested frequencies while W_{rec} is the smallest because of the wide loop, and η is only 85.31%. However, at other frequencies from 1 to 100 Hz, W_{rec} increases from 12.44 to 12.86 J/cm^3, corresponding to a variation of less than 3.4%, while η remains above 91%. Overall, the PLSBZST2 ceramics exhibit excellent temperature and frequency stabilities over the measured ranges, indicating their potential for use in pulse power capacitor applications.

Moreover, it was observed that the thickness of the ceramic was closely related to the energy storage density. For example, an energy storage density W_{rec} of 20.09 J/cm^3 was obtained at 1,440 kV/cm for a PLSBZST2 ceramic with a thickness of 7.00 ± 0.20 μm. In our previous studies, W_{rec} was 12.9 J/cm^3 at 570 kV/cm for a $(PbBaSrLa)(ZrSn)O_3$ ceramic with a thickness of 32 μm[54], 9.84 J/cm^3 at 440 kV/cm for a $(PbLa)(ZrSn)O_3$ ceramic with a thickness of 50 μm[61], and 5.72 J/cm^3 at 280 kV/cm for $(PbLa)(ZrSnHf)O_3$ ceramic with a thickness of 50-70 μm[62]. The energy storage density increases with decreasing thickness in thick-film ceramics. The thickness dependence of the energy storage density reminds us of the general relationship of energy storage density as a function of thickness. Especially whether or not we can figure out a mathematical relation to describe this kind of relation. Furthermore, the thickness dependences of polarization, especially

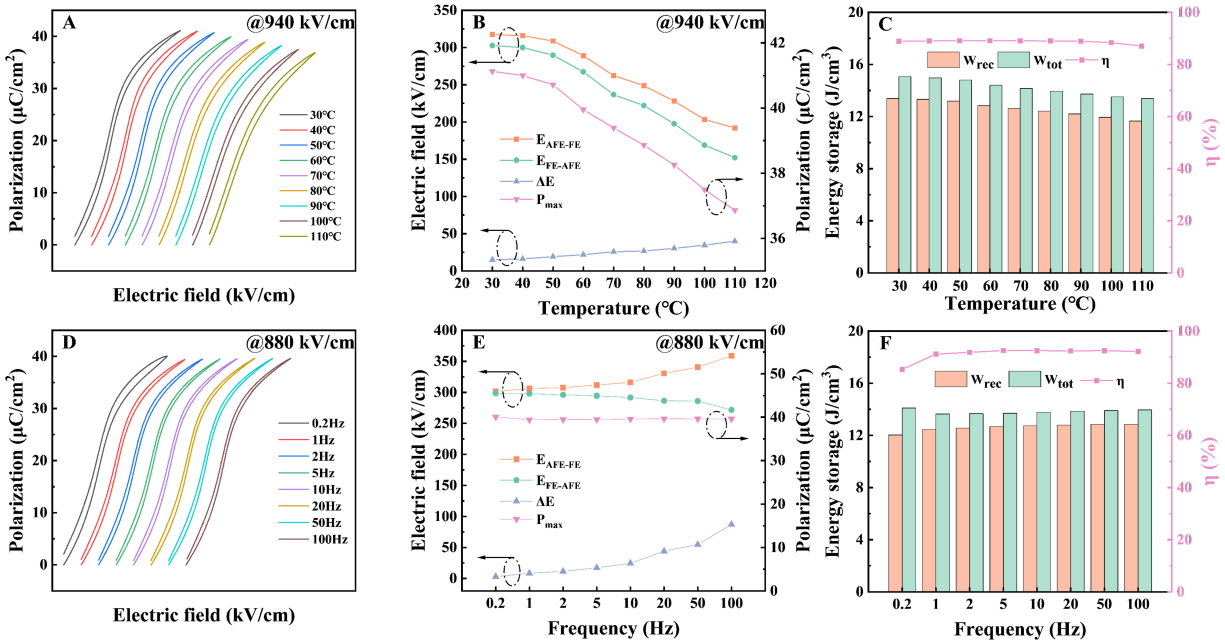


Figure 6. (A) P-E loops for PLSBZST2 thick-film ceramics at 940 kV/cm from 30 to 110 °C; (B) Corresponding E_{AFE-FE}, E_{FE-AFE}, ΔE, and P_{max} values obtained at various temperatures; (C) Calculated W_{tot}, W_{rec}, and η values obtained at various temperatures; (D) P-E loops for the PLSBZST2 thick-film ceramic at 880 kV/cm from 0.2 to 100 Hz; (E) Corresponding E_{AFE-FE}, E_{FE-AFE}, ΔE, and P_{max} obtained at various frequencies; (F) Calculated W_{tot}, W_{rec}, and η values obtained at various frequencies. P-E: Polarization - electric field; PLSBZST2: $(Pb_{0.86}La_{0.04}Sr_{0.06}Ba_{0.02})(Zr_{0.64}Sn_{0.35}Ti_{0.01})O_3$; P_{max}: maximum polarization; W_{tot}: total energy storage density; W_{rec}: recoverable energy storage density.

the maximum polarization and DBS, might also be figured out. In fact, the DBS may be related to the thickness via the Gerson-Marshall relation[63]:

$$E_{DBS} = 27.2t^{-0.39} \tag{7}$$

where t is in cm and E_{DBS} is in kV/cm.

In general, E_{DBS} can be written as

$$E_{DBS} \sim t^{s1} \tag{8}$$

where $s1$ is a constant, -0.39. Because the polarization is proportional to the electric field, $P = \varepsilon_r\varepsilon_0 E$ for linear ferroelectrics (ε_0 is the vacuum dielectric constant) and $P \sim E^2$ for nonlinear ferroelectrics (i.e., via the Rayleigh relation and even higher powers[64]), the polarization remains an exponential function:

$$P_{max} \sim t^{s2} \tag{9}$$

where $s2$ is also a constant. The recoverable energy storage density is defined as Equation (2) i.e., $W_{rec} = \int EdP$. Here, because energy storage density is the product of electric field times the polarization, while both the electric field and the polarization have an exponential relationship with the thickness, thereby the energy storage density has an exponential relationship with the thickness, no matter the ferroelectric is a linear

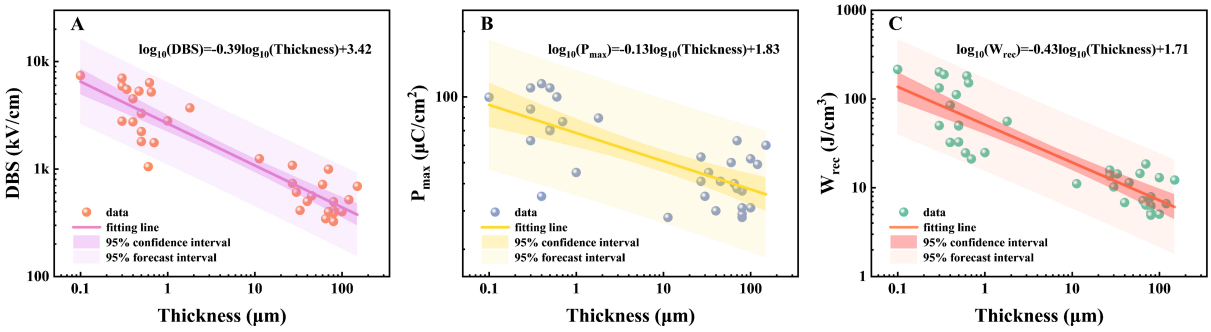


Figure 7. Fitted results of the DBS (A)[65-69], P_{max} (B)[70-74] and W_{rec} (C)[75-79] values as a function of thickness[80-84] for data extracted from the literature[11,31,33-35,41-43,55,56,85-89,90-93]. DBS: Dielectric breakdown strength; P_{max}: maximum polarization; W_{rec}: recoverable energy storage density.

ferroelectric (*P vs. E*), or a nonlinear ferroelectric [*P vs.* E^2 for Rayleigh relationship, or *P vs.* E^n ($n > 2$)][28]. Therefore, the recoverable energy storage density exhibits an exponential relationship with the thickness via

$$W_{rec} \sim t^{s0} \tag{10}$$

where *s*0 is still a constant. Because W_{rec} is the product of the polarization and the electric field, there exists the following relationship among *s*0, *s*1, and *s*2:

$$s0 = s1 + s2 \tag{11}$$

We compared the data obtained with this study with DBS (a)[65-69], P_{max} (b)[70-74], and W_{rec} (c)[75-79] data obtained in previous studies as a function of thickness[80-84] for bulk ceramics, thick film ceramics, and thin films (see Supplementary Table 1)[11,31,33-35,41-43,55,56,85-93]. The data were then fitted using Equations (8)-(10), and the results are shown in Figure 7A-C. We obtained *s*1, *s*2, and *s*0 values of -0.39 ± 0.03, -0.13 ± 0.03, and -0.43 ± 0.04, respectively. Here, *s*0 is notably less than the sum of *s*1 and *s*2, which likely resulted from the small polarization and electric field used to measure the recoverable energy storage density, because usually the applied electric field used for measuring the recoverable energy storage density is smaller than the DBS, and the polarization obtained at an electric field less than the DBS is smaller than the maximum polarization, and the larger the electric field, the larger the maximum polarization, the DBS and the recoverable energy storage density. Therefore, the absolute value of *s*0 will be less than the absolute sum of *s*1 + *s*2. For example, if less than 10% of each parameter is used, then a 20% error will be generated. Therefore, an *s*0 value of -0.42 will be obtained, which is similar to the actual *s*0 value of -0.43. In addition, it should be noted that the *s*1 value obtained here (-0.39) is the same as that obtained using Equation (7)[63].

The nominal energy density can be calculated by integrating the electric field with respect to the polarization for the P-E hysteresis loop. Therefore, the actual charging and discharging performance of ceramics can be evaluated using the resistor-inductor-capacitor (R-L-C) circuit[30,94,95]. According to the different circuit parameters, the circuit can be divided into an underdamped circuit and an overdamped circuit depending on the load. In an underdamped circuit, the pulse capacitor can release a higher current and thus a higher power density. In an overdamped circuit, the energy stored in the ceramic capacitor can be fully released[43], which is beneficial for analyzing the actual discharge performance of the ceramics. Figure 8A shows the discharged current as a function of time for the PLSBZST2 thick-film ceramic obtained under different electric fields in the overdamped circuit. The peak current gradually increases with increasing electric field. The discharged energy density (W_{dis}) may be defined as a function of time for different electric fields during charging, as shown in Figure 8B. In general, W_{dis} can be calculated via[96]

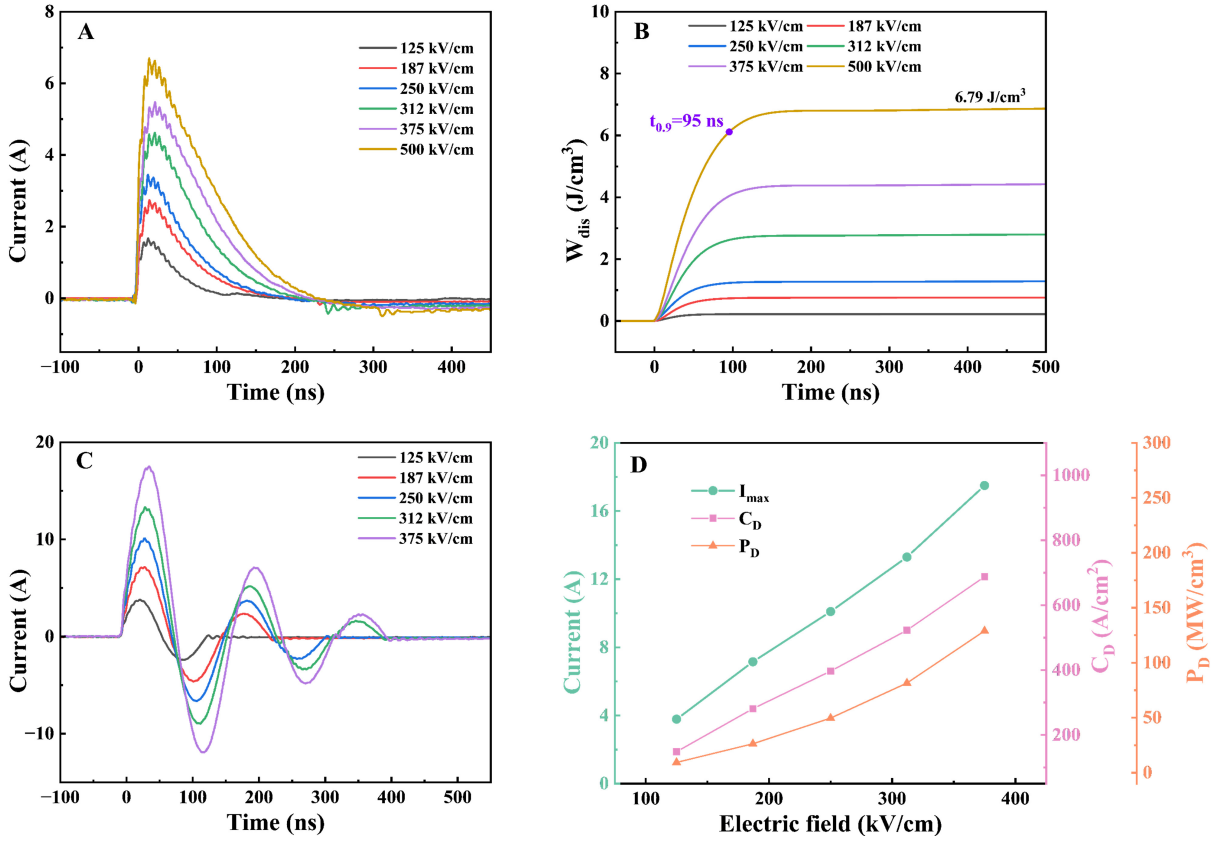


Figure 8. Discharge current as a function of time for the PLSBZST2 thick-film ceramic. (A) Overdamped discharge current obtained under various electric fields; (B) Corresponding W_{dis} values obtained under various electric fields; (C) Underdamped discharge current obtained under various electric fields; (D) Corresponding I_{max}, C_D, and P_D values as a function of the electric field. I_{max}: Peak current; PLSBZST2: $(Pb_{0.86}La_{0.04}Sr_{0.06}Ba_{0.02})(Zr_{0.64}Sn_{0.35}Ti_{0.01})O_3$; C_D: discharged current density; P_D: discharged power density; W_{dis}: discharged energy density.

$$W_{dis} = \frac{R\int i(t)^2 dt}{v} \tag{12}$$

where R is the total resistance in the overdamped circuit (here, R = 100 Ω), $i(t)$ is the discharged current, and v is the effective volume of the sample under test. Therefore, W_{dis} increases with increasing electric field. When the electric field approaches 312 kV/cm near the transition field $E_{AFE\text{-}FE}$, W_{dis} rapidly increases, and the maximum W_{dis} value of 6.79 J/cm³ is obtained at 500 kV/cm. The discharge time ($t_{0.9}$) is defined as the time required to reach 90% of the discharged energy density W_{dis}[97]. At an electric field of 500 kV/cm, the PLSBZST2 ceramics can release 90% of W_{dis} in 95 ns, demonstrating rapid discharge. Figure 8C shows the discharged current as a function of time for the PLSBZST2 ceramic under different electric fields in an underdamped state. Here, the peak current (I_{max}) increases with increasing electric field. The oscillatory pulse current can be evaluated in terms of the discharged current density (C_D) and power density (P_D)[98]:

$$C_D = \frac{I_{max}}{S} \tag{13}$$

$$P_D = \frac{EI_{max}}{2S} \tag{14}$$

where I_{max} is the peak value of the first pulse current, E is the charging electric field, and S is the electrode area of the sample. I_{max}, C_D, and P_D are shown as functions of the electric field in Figure 8D. Here, I_{max}, C_D, and P_D monotonically increase with increasing electric field, and a pronounced increase occurs near the AFE-FE transition field. The maximum C_D and P_D values of 687.73 A/cm² and 128.95 MW/cm³, respectively, are

obtained under an electric field of 375 kV/cm. These results demonstrate that the PLSBZST2 ceramic exhibits a high discharged energy density, high discharged current, high power density, and short discharge time, indicating its potential for application in pulse-power devices.

CONCLUSIONS

In this study, $(Pb_{0.92-x}La_{0.04}Sr_xBa_{0.02})(Zr_{0.64}Sn_{0.35}Ti_{0.01})O_3$ (PLSBZST; x = 0.04, 0.06, 0.08 and 0.10) freestanding thick-film ceramics were successfully fabricated using the tape-casting process. The results show that the forward AFE-FE switching field and relaxor degree increase with increasing Sr^{2+} content, while a fine grain size and dense microstructure are beneficial for improving the DBS. In particular, the PLSBZST2 thick-film ceramic demonstrated a maximum W_{rec} of 20.09 J/cm^3 with an η of 91.34% at 1,440 kV/cm, together with excellent frequency and temperature stabilities and an excellent discharging performance. In addition, under a load of 100 Ω, the PLSBZST2 ceramic exhibited a maximum W_{dis} value of 6.79 J/cm^3 at 500 kV/cm and released 90% of this W_{dis} value within 95 ns. Moreover, maximum C_D and P_D values of 687.73 A/cm^2 and 128.95 MW/cm^3 were obtained. These findings indicate the potential of PLSBZST thick-film ceramics for use in pulse-power devices. Moreover, reciprocal exponential relationships of the maximum polarization, DBS, and W_{rec} as a function of the sample thickness were obtained. The $s2$, $s1$, and $s0$ exponents associated with these relationships were -0.13 ± 0.03, -0.39 ± 0.03, and -0.43 ± 0.04, respectively. Here, the value of exponent $s1$ is the same as that obtained using the Gerson-Marshall equation, and $s0$ is almost equal to ($s1$ + $s2$) 80%, which results from using 10% less than the maximum polarization and a lower electric field than that used for the DBS due to the lower electric field that was employed during measurement. The thickness dependence of the recoverable energy storage density directly indicates that the reduction on the thickness of the ceramic layer will be one of the important approaches to enhance the energy storage density for the pulse power capacitors.

DECLARATIONS

Authors' contributions

Conception and design: Lu, S. G.; Wang, S.; Yan, X.

Experiments, data collection and analysis, data curation: Yan, X.; Yu, C.; Li, Y.

Writing of the original draft: Yan, X.; Wang, S.

Writing - review and editing: Lu, S. G.; Gao, X.; Wang, S.; Yao, Y.; Tao, T.; Liang, B.; Gong, W.; Niu, X.; Jian, X.

Supervision, project administration and funding acquisition: Lu, S. G.; Gao, X.; Jian, X.

Availability of data and materials

The data supporting the findings of this study are available within this Article and its Supplementary Materials. Further data are available from the corresponding authors upon request.

AI and AI-assisted tools statement

Not applicable.

Financial support and sponsorship

This work was supported by the Natural Science Foundation of China (Grant Nos. 52272105, 52202130, 52402161), the NSFC-Guangdong Joint Fund (Grant No. U1501246), the State Key Laboratory of Precision Electronic Manufacturing Technology and Equipment-opening fund (JMDZ202305), the Dongguan City Frontier Research Project (2019622101006), the Advanced Energy Science and Technology Guangdong Provincial Laboratory Foshan Branch-Foshan Xianhu Laboratory Open Fund-Key Project (Grant No. XHT2020-011), the Open Projects of the Guangdong Provincial Key Laboratory of Electronic Functional Materials and Devices, Huizhou University [grant numbers EFMD2022004Z and EFMD2024007Z], the Open Project of the Guangdong Provincial Key Laboratory of Energy Conversion Materials and Technology, Guangdong Technion-Israel Institute of Technology [MATEC2024KF003], and the Taishan Industrial Experts Program [No. tscx202507141].

Conflicts of interest

Gao, X. is affiliated with Shandong Industrial Ceramics Research and Design Institute Co., Ltd. The other authors declared that there are no conflicts of interest.

Ethical approval and consent to participate

Not applicable.

Consent for publication

Not applicable.

Copyright

© The Author(s) 2026.

Supplementary Materials

Supplementary Materials

REFERENCES

1. Hao, X.; Zhai, J.; Kong, L. B.; Xu, Z. A comprehensive review on the progress of lead zirconate-based antiferroelectric materials. *Prog. Mater. Sci.* **2014**, *63*, 1-57. DOI
2. Zhang, L.; Jing, R.; Zhang, S.; Jin, L. Multiscale microstructure design for high-performance dielectric energy storage materials. *Microstructures* **2026**, *6*, 2026002. DOI
3. Luo, N.; Ma, L.; Luo, G.; et al. Well-defined double hysteresis loop in $NaNbO_3$ antiferroelectrics. *Nat. Commun.* **2023**, *14*, 1776. DOI PubMed PMC
4. You, Y.; Fang, G.; Fan, M.; Guo, J.; Li, Q.; Wan, J. Leveraging novel microwave techniques for tailoring the microstructure of energy storage materials. *Microstructures* **2024**, *4*, 2024035. DOI
5. Randall, C. A.; Fan, Z.; Reaney, I.; Chen, L. Q.; Trolier-McKinstry, S. Antiferroelectrics: history, fundamentals, crystal chemistry, crystal structures, size effects, and applications. *J. Am. Ceram. Soc.* **2021**, *104*, 3775-810. DOI
6. Tan, X.; Ma, C.; Frederick, J.; Beckman, S.; Webber, K. G. The antiferroelectric ↔ ferroelectric phase transition in lead-containing and lead-free perovskite ceramics. *J. Am. Ceram. Soc.* **2011**, *94*, 4091-107. DOI
7. Zhao, L.; Liu, Q.; Gao, J.; Zhang, S.; Li, J. F. Lead-free antiferroelectric silver niobate tantalate with high energy storage performance. *Adv. Mater.* **2017**, *29*, 1701824. DOI
8. Luo, N.; Han, K.; Cabral, M. J.; et al. Constructing phase boundary in $AgNbO_3$ antiferroelectrics: pathway simultaneously achieving high energy density and efficiency. *Nat. Commun.* **2020**, *11*, 4824. DOI PubMed PMC
9. Wang, J.; Shen, Z. Modeling-guided understanding microstructure effects in energy storage dielectrics. *Microstructures.* **2021**, *1*, 2021006. DOI
10. Gao, J.; Zhang, Y.; Zhao, L.; et al. Enhanced antiferroelectric phase stability in La-doped $AgNbO_3$: perspectives from the microstructure to energy storage properties. *J. Mater. Chem. A.* **2019**, *7*, 2225-32. DOI
11. Wang, X.; Zhu, Q.; Sun, H.; et al. Ultrahigh energy storage density and efficiency in PLZST antiferroelectric ceramics via multiple optimization strategy. *J. Eur. Ceram. Soc.* **2023**, *43*, 4051-9. DOI
12. Yao, Z.; Song, Z.; Hao, H.; et al. Homogeneous/inhomogeneous-structured dielectrics and their energy-storage performances. *Adv. Mater.* **2017**, *29*, 1601727. DOI
13. Guo, J.; Yang, T. Giant energy storage density in Ba, La co-doped $PbHfO_3$-based antiferroelectric ceramics by a rolling process. *J. Alloys. Compd.* **2021**, *888*, 161539. DOI
14. Jiang, Y.; Zhu, C.; Zhao, P.; et al. Excellent energy storage performance of $NaNbO_3$-based antiferroelectric ceramics with ultrafast charge/discharge rate. *J. Eur. Ceram. Soc.* **2021**, *41*, 6465-73. DOI
15. Lin, Z.; Chen, Y.; Liu, Z.; Wang, G.; Rémiens, D.; Dong, X. Large energy storage density, low energy loss and highly stable $(Pb_{0.97}La_{0.02})(Zr_{0.66}Sn_{0.23}Ti_{0.11})O_3$ antiferroelectric thin-film capacitors. *J. Eur. Ceram. Soc.* **2018**, *38*, 3177-81. DOI
16. Sun, N.; Du, J.; Zhao, Y.; et al. Flexible multilayer lead-free film capacitor with high energy storage performances via heterostructure engineering. *J. Materiomics.* **2022**, *8*, 772-80. DOI
17. Palneedi, H.; Peddigari, M.; Hwang, G. T.; Jeong, D. Y.; Ryu, J. High-performance dielectric ceramic films for energy storage capacitors: progress and outlook. *Adv. Funct. Mater.* **2018**, *28*, 1803665. DOI
18. Yang, L.; Kong, X.; Li, F.; et al. Perovskite lead-free dielectrics for energy storage applications. *Prog. Mater. Sci.* **2019**, *102*, 72-108. DOI

19. Li, Y.; Gao, J.; Yang, T. Excellent energy density and efficiency in Ba and Sr co-doped (Pb,La)(Zr,Sn)O_3 antiferroelectric ceramics. *J. Phys. Chem. Solids.* **2023**, *172*, 111046. DOI
20. Pattipaka, S.; Lim, Y.; Son, Y. H.; Bae, Y. M.; Peddigari, M.; Hwang, G. Ceramic-based dielectric materials for energy storage capacitor applications. *Materials* **2024**, *17*, 2277. DOI PubMed PMC
21. Wang, X.; Shen, J.; Yang, T.; Dong, Y.; Liu, Y. High energy-storage performance and dielectric properties of antiferroelectric $(Pb_{0.97}La_{0.02})(Zr_{0.5}Sn_{0.5-x}Ti_x)O_3$ ceramic. *J. Alloys. Compd.* **2016**, *655*, 309-13. DOI
22. Wang, X.; Yang, T.; Shen, J. High-energy storage performance in $(Pb_{0.98}La_{0.02})(Zr_{0.45}Sn_{0.55})_{0.995}O_3$ AFE thick films fabricated via a rolling process. *J. Am. Ceram. Soc.* **2016**, *99*, 3569-72. DOI
23. Zhang, Y.; Liu, P.; Shen, M.; et al. High energy storage density of tetragonal PBLZST antiferroelectric ceramics with enhanced dielectric breakdown strength. *Ceram. Int.* **2020**, *46*, 3921-6. DOI
24. Huang, K.; Ge, G.; Bai, H.; et al. Ameliorative energy-storage properties stemmed from the refined grains in PBLZS antiferroelectric ceramics via introducing liquid phase sintering. *J. Eur. Ceram. Soc.* **2021**, *41*, 2450-7. DOI
25. Mohapatra, P.; Fan, Z.; Cui, J.; Tan, X. Relaxor antiferroelectric ceramics with ultrahigh efficiency for energy storage applications. *J. Eur. Ceram. Soc.* **2019**, *39*, 4735-42. DOI
26. Fu, Z.; Chen, X.; Li, Z.; et al. Unveiling the ferrielectric nature of $PbZrO_3$-based antiferroelectric materials. *Nat. Commun.* **2020**, *11*, 3809. DOI PubMed PMC
27. Ge, P.; Tang, X.; Meng, K.; et al. Ultrahigh energy storage density and superior discharge power density in a novel antiferroelectric lead hafnate. *Mater. Today. Phys.* **2022**, *24*, 100681. DOI
28. Zhao, P.; Wang, S.; Tang, H.; et al. Superior energy storage density and giant negative electrocaloric effects in $(Pb_{0.98}La_{0.02})(Zr, Sn)O_3$ antiferroelectric ceramics. *Scr. Mater.* **2021**, *200*, 113920. DOI
29. Liu, X.; Li, Y.; Hao, X. Ultra-high energy-storage density and fast discharge speed of $(Pb_{0.98-x}La_{0.02}Sr_x)(Zr_{0.9}Sn_{0.1})_{0.995}O_3$ antiferroelectric ceramics prepared *via* the tape-casting method. *J. Mater. Chem. A.* **2019**, *7*, 11858-66. DOI
30. Liu, X.; Yang, T.; Gong, W. Achieving ultrahigh energy-storage capability in $PbZrO_3$-based antiferroelectric capacitors based on optimization of property parameters. *J. Mater. Chem. A.* **2022**, *10*, 4137-45. DOI
31. Liu, X.; Zhao, Y.; Sun, N.; Li, Y.; Hao, X. Ultra-high energy density induced by diversified enhancement effects in $(Pb_{0.98-x}La_{0.02}Ca_x)(Zr_{0.7}Sn_{0.3})_{0.99}5O_3$ antiferroelectric multilayer ceramic capacitors. *Chem. Eng. J.* **2021**, *417*, 128032. DOI
32. Liu, X.; Yang, T.; Gong, W. Comprehensively enhanced energy-storage properties in $(Pb_{1-3x/2}La_x)(Zr_{0.995}Ti_{0.005})O_3$ antiferroelectric ceramics *via* composition optimization. *J. Mater. Chem. C.* **2021**, *9*, 12399-407. DOI
33. Niu, X.; Jiang, Y.; Liang, W.; et al. Boosted energy storage densities in lead-free $Na_{0.5}Bi_{0.5}TiO_3$-based thick film ceramics via the compositional and microstructural tailoring. *Chem. Eng. J.* **2024**, *496*, 154047. DOI
34. Li, C.; Yao, M.; Yang, T.; Yao, X. Optimizing energy storage performance of lead zirconate-based antiferroelectric ceramics by a phase modulation strategy. *Chem. Eng. J.* **2024**, *497*, 154913. DOI
35. Li, Y.; Hu, T.; Chen, X.; Xie, J.; Shi, Y. Achieving high energy storage performance in $PbHfO_3$-based antiferroelectric ceramics by Sr element doping. *J. Alloys. Compd.* **2024**, *994*, 174651. DOI
36. Wang, X.; Shen, J.; Yang, T.; Xiao, Z.; Dong, Y. Phase transition and energy storage performance in Ba-doped PLZST antiferroelectric ceramics. *J. Mater. Sci. Mater. Electron.* **2015**, *26*, 9200-4. DOI
37. Zhang, Q.; Liu, X.; Zhang, Y.; et al. Effect of barium content on dielectric and energy storage properties of (Pb,La,Ba)(Zr,Sn,Ti)O_3 ceramics. *Ceram. Int.* **2015**, *41*, 3030-5. DOI
38. Meng, X.; Zhao, Y.; Li, Y.; Hao, X. Systematical investigation on energy-storage behavior of PLZST antiferroelectric ceramics by composition optimizing. *J. Am. Ceram. Soc.* **2021**, *104*, 2170-80. DOI
39. Breval, E.; Wang, C.; Dougherty, J. P.; Gachigi, K. W. PLZT phases near lead zirconate: 1. determination by X-ray diffraction. *J. Am. Ceram. Soc.* **2005**, *88*, 437-42. DOI
40. Xing, Z.; Feng, Y.; Wei, X. Effect of Sn content on dielectric, piezoelectric and ferroelectric properties for $Pb(Zr_{0.35}Ti_{0.65})_{1-x}Sn_xO_3$ ceramics near morphotropic phase boundary. *J. Alloys. Compd.* **2015**, *627*, 238-43. DOI
41. Qi, H.; Zuo, R.; Xie, A.; et al. Ultrahigh energy-storage density in $NaNbO_3$-based lead-free relaxor antiferroelectric ceramics with nanoscale domains. *Adv. Funct. Mater.* **2019**, *29*, 1903877. DOI
42. Liu, H.; Niu, X.; Wang, T.; et al. Superior energy storage properties in lead-free $NaNbO_3$-based relaxor antiferroelectric ceramics*via*a combined optimization strategy. *J. Mater. Chem. C.* **2024**, *12*, 3962-71. DOI
43. Yu, C.; Wang, S.; Yan, X.; et al. Excellent energy storage and charge-discharge performance in $(Pb_{1-x}Ca_x)(Zr_{0.55}Sn_{0.45})O_3$ antiferroelectric ceramics. *ACS. Appl. Mater. Interfaces.* **2025**, *17*, 5066-77. DOI

44. He, H.; Tan, X. Electric-field-induced transformation of incommensurate modulations in antiferroelectric $Pb_{0.99}Nb_{0.02}[(Zr_{1-x}Sn_x)_{1-y}Tiy]_{0.98}O_3$. *Phys. Rev. B.* **2005**, *72*, 024102. DOI
45. Tunkasiri, T.; Rujijanagul, G. Dielectric strength of fine grained barium titanate ceramics. *J. Mater. Sci. Lett.* **1996**, *15*, 1767-9. DOI
46. Zhao, M.; Shen, X.; Wang, J.; Wang, J.; Zhang, J.; Zhao, L. Superior comprehensive energy storage performances in Eu-doped $AgNbO_3$ antiferroelectric ceramics. *Chem. Eng. J.* **2023**, *478*, 147527. DOI
47. Zhang, Q.; Dan, Y.; Chen, J.; et al. Effects of composition and temperature on energy storage properties of (Pb,La)(Zr,Sn,Ti)O_3 antiferroelectric ceramics. *Ceram. Int.* **2017**, *43*, 11428-32. DOI
48. Gao, H.; Sun, N.; Li, Y.; et al. Enhanced electrocaloric effect and energy-storage performance in PBLZT films with various Ba^{2+} content. *Ceram. Int.* **2016**, *42*, 16439-47. DOI
49. Xu, R.; Xu, Z.; Feng, Y.; Tian, J.; Huang, D. Energy storage and release properties of Sr-doped (Pb,La)(Zr,Sn,Ti)O_3 antiferroelectric ceramics. *Ceram. Int.* **2016**, *42*, 12875-9. DOI
50. Luo, Y.; Han, B.; Fu, Z.; et al. High polarization stability of Sr modified Pb(Zr,Sn)NbO_3 antiferroelectric ceramics. *J. Am. Ceram. Soc.* **2022**, *105*, 6765-74. DOI
51. Wang, H.; Liu, Y.; Yang, T.; Zhang, S. Ultrahigh energy-storage density in antiferroelectric ceramics with field-induced multiphase transitions. *Adv. Funct. Mater.* **2019**, *29*, 1807321. DOI
52. Yang, Y.; Liu, P.; Zhang, Y.; et al. Low electric-field-induced strain and high energy storage efficiency in (Pb,Ba,La)(Zr,Sn,Ti)O_3 antiferroelectric ceramics through regulating the content of La. *Ceram. Int.* **2020**, *46*, 18106-13. DOI
53. Wang, S.; Zhao, P.; Jian, X.; et al. Large energy storage density and electrocaloric strength of $Pb_{0.97}La_{0.02}(Zr_{0.46-x}Sn_{0.54}Ti_x)O_3$ antiferroelectric thick film ceramics. *Scr. Mater.* **2022**, *210*, 114426. DOI
54. Wang, S.; Li, W.; Yu, Y.; et al. Ultra-high energy storage density in PBSLZS antiferroelectric thick film ceramics. *Scr. Mater.* **2024**, *252*, 116287. DOI
55. Meng, X.; Zhao, Y.; Li, Y.; Hao, X. Simultaneously achieving ultrahigh energy density and power density in $PbZrO_3$-based antiferroelectric ceramics with field-induced multistage phase transition. *J. Alloys. Compd.* **2021**, *868*, 159149. DOI
56. Hu, J.; Wang, W.; Yang, Y.; et al. Achieving ultrahigh energy storage performance of PBLZST-based antiferroelectric composite ceramics via interfacial polarization engineering. *J. Eur. Ceram. Soc.* **2024**, *44*, 7642-50. DOI
57. Ma, J.; Zhang, J.; Guo, J.; et al. Achieving ultrahigh energy storage density in lead-free sodium niobate-based ceramics by modulating the antiferroelectric phase. *Chem. Mater.* **2022**, *34*, 7313-22. DOI
58. Bi, W.; Li, L.; Tian, G.; et al. Comprehensive energy-storage performance enhancement in relaxor anti-ferroelectrics via strengthening local polarization. *Chem. Eng. J.* **2023**, *478*, 147383. DOI
59. Chen, L.; Zhou, J.; Xu, L.; et al. Achieving ultra-short discharge time and high energy density in lead-based antiferroelectric ceramics by A-site substitution. *Chem. Eng. J.* **2022**, *447*, 137367. DOI
60. Liu, X.; Li, Y.; Li, Y.; Hao, X. Giant energy-storage density and thermally activated phase transition in $(Pb_{0.96}La_{0.04})(Zr_{0.99}Ti_{0.01})O_3$ antiferroelectric ceramics. *ACS. Appl. Energy. Mater.* **2021**, *4*, 4897-902. DOI
61. Wang, S.; Chen, X.; Jian, X.; et al. High energy-storage density and giant negative electrocaloric effect in PLZS antiferroelectric thick film ceramics prepared via the tape-casting process. *J. Alloys. Compd.* **2024**, *996*, 174724. DOI
62. Li, W.; Wang, S.; Lin, C.; et al. Enhanced energy-storage density in $(Pb0.98La0.02)(Zr_{0.45-x}Sn_{0.55}Hf_x)_{0.995}O_3$ antiferroelectric ceramics. *Scr. Mater.* **2024**, *242*, 115959. DOI
63. Gerson, R.; Marshall, T. C. Dielectric breakdown of porous ceramics. *J. Appl. Phys.* **1959**, *30*, 1650-3. DOI
64. Hall, D. A.; Stevenson, P. J. High field dielectric behaviour of ferroelectric ceramics. *Ferroelectrics* **1999**, *228*, 138-58. DOI
65. Shi, M.; Pan, X.; Lin, D.; et al. Localized chemical disorder induced superior energy storage performance of $PbZrO_3$-based antiferroelectric ceramics. *Chem. Eng. J.* **2025**, *514*, 163459. DOI
66. Hu, P.; Yao, M.; Yang, T.; Yao, X. Ultrahigh energy storage density and efficiency achieved in $PbZrO_3$-based antiferroelectric ceramics via phase modulation engineering. *ACS. Appl. Mater. Interfaces.* **2025**, *17*, 26881-91. DOI
67. Chen, L.; Li, Y.; Zhang, Q.; Hao, X. Electrical properties and energy-storage performance of $(Pb_{0.92}Ba_{0.05}La_{0.02})(Zr_{0.68}Sn_{0.27}Ti_{0.05})O_3$ antiferroelectric thick films prepared by tape-casing method. *Ceram. Int.* **2016**, *42*, 12537-42. DOI
68. Jiang, J.; Meng, X.; Li, L.; et al. Ultrahigh energy storage density in lead-free relaxor antiferroelectric ceramics via domain engineering. *Energy. Storage. Mater.* **2021**, *43*, 383-90. DOI
69. Wang, X.; Zhao, H.; Tang, M.; et al. Samarium-modified PLZST-based antiferroelectric energy storage ceramics for low-temperature sintering in reducing atmosphere. *Ceram. Int.* **2024**, *50*, 21736-44. DOI
70. Wang, X.; Sun, H.; Wang, M.; et al. Low-temperature sintering of PLSZT-based antiferroelectric ceramics in reducing atmosphere for energy storage. *J. Eur. Ceram. Soc.* **2024**, *44*, 898-906. DOI

71. Ye, W.; Zhu, C.; Xiao, Y.; et al. Remarkable energy-storage performances and excellent stability in $CaTiO_3$-doped $BiFeO_3$-$BaTiO_3$ relaxor ferroelectric ceramics. *J. Eur. Ceram. Soc.* **2023**, *43*, 900-8. DOI
72. Deng, T.; Liu, Z.; Hu, T.; Dai, K.; Hu, Z.; Wang, G. Excellent energy-storage performance in $Bi_{0.5}Na_{0.5}TiO_3$-based lead-free composite ceramics via introducing pyrochlore phase $Sm_2Ti_2O_7$. *Chem. Eng. J.* **2023**, *465*, 142992. DOI
73. Che, Z.; Ma, L.; Luo, G.; et al. Phase structure and defect engineering in $(Bi_{0.5}Na_{0.5})TiO_3$-based relaxor antiferroelectrics toward excellent energy storage performance. *Nano. Energy.* **2022**, *100*, 107484. DOI
74. Nguyen, M. D. Effect of substrate and electrode on the crystalline structure and energy storage performance of antiferroelectric $PbZrO_3$ films. *Thin. Solid. Films.* **2021**, *717*, 138441. DOI
75. Chen, Q.; Zhang, Y.; Zhang, J.; et al. Effects of Ti-doping on energy storage properties and cycling stability of $Pb_{0.925}La_{0.05}ZrO_3$ antiferroelectric thin films. *Mater. Sci. Eng. B.* **2022**, *286*, 116024. DOI
76. Li, Y. Z.; Wang, Z. J.; Bai, Y.; Zhang, Z. D. High energy storage performance in Ca-doped $PbZrO_3$ antiferroelectric films. *J. Eur. Ceram. Soc.* **2020**, *40*, 1285-92. DOI
77. Yang, F.; Shi, Y. J.; Lin, L.; et al. Improvement of energy storage performance in $PbZr_{0.52}Ti_{0.48}O_3$/$PbZrO_3$ multilayer thin films via regulating $PbZrO_3$ thickness. *Curr. Appl. Phys.* **2023**, *50*, 145-52. DOI
78. Cai, H.; Yan, S.; Dong, X.; Cao, F.; Wang, G. Significantly enhanced energy storage performance by constructing TiO_2 nanowire arrays in $PbZrO_3$-based antiferroelectric films. *Ceram. Int.* **2020**, *46*, 6436-42. DOI
79. Ahn, C. W.; Amarsanaa, G.; Won, S. S.; Chae, S. A.; Lee, D. S.; Kim, I. W. Antiferroelectric thin-film capacitors with high energy-storage densities, low energy losses, and fast discharge times. *ACS. Appl. Mater. Interfaces.* **2015**, *7*, 26381-6. DOI PubMed
80. Chen, T.; Wang, J.; Zhong, X.; Wang, F.; Li, B.; Zhou, Y. High energy density capacitors based on $0.88BaTiO_3$-$0.12Bi(Mg_{0.5},Ti_{0.5})O_3$/$PbZrO_3$ multilayered thin films. *Ceram. Int.* **2014**, *40*, 5327-32. DOI
81. Zhang, J.; Zhang, Y.; Chen, Q.; et al. Enhancement of energy-storage density in PZT/PZO-based multilayer ferroelectric thin films. *Nanomaterials.* **2021**, *11*, 2141. DOI PubMed PMC
82. Ma, B.; Hu, Z.; Koritala, R. E.; Lee, T. H.; Dorris, S. E.; Balachandran, U. PLZT film capacitors for power electronics and energy storage applications. *J. Mater. Sci:. Mater. Electron.* **2015**, *26*, 9279-87. DOI
83. Park, M. H.; Kim, H. J.; Kim, Y. J.; Moon, T.; Kim, K. D.; Hwang, C. S. Thin $Hf_xZr_{1-x}O_2$ films: a new lead-free system for electrostatic supercapacitors with large energy storage density and robust thermal stability. *Adv. Energy. Mater.* **2014**, *4*, 1400610. DOI
84. Sun, Z.; Ma, C.; Liu, M.; et al. Ultrahigh energy storage performance of lead-free oxide multilayer film capacitors via interface engineering. *Adv. Mater.* **2016**, *29*, 1604427. DOI
85. Hao, X.; Wang, Y.; Zhang, L.; Zhang, L.; An, S. Composition-dependent dielectric and energy-storage properties of $(Pb,La)(Zr,Sn,Ti)O_3$ antiferroelectric thick films. *Appl. Phys. Lett.* **2013**, *102*, 163903. DOI
86. Yang, B.; Zhang, Y.; Pan, H.; et al. High-entropy enhanced capacitive energy storage. *Nat. Mater.* **2022**, *21*, 1074-80. DOI
87. Shu, L.; Shi, X.; Zhang, X.; et al. Partitioning polar-slush strategy in relaxors leads to large energy-storage capability. *Science* **2024**, *385*, 204-9. DOI
88. Pan, H.; Lan, S.; Xu, S.; et al. Ultrahigh energy storage in superparaelectric relaxor ferroelectrics. *Science* **2021**, *374*, 100-4. DOI
89. Kim, J.; Saremi, S.; Acharya, M.; et al. Ultrahigh capacitive energy density in ion-bombarded relaxor ferroelectric films. *Science* **2020**, *369*, 81-4. DOI
90. Pan, H.; Li, F.; Liu, Y.; et al. Ultrahigh-energy density lead-free dielectric films via polymorphic nanodomain design. *Science* **2019**, *365*, 578-82. DOI
91. Liu, Y.; Zhang, Y.; Wang, J.; et al. Ultrahigh capacitive energy storage through dendritic nanopolar design. *Science* **2025**, *388*, 211-6. DOI
92. Han, S.; Kim, J. S.; Park, E.; et al. High energy density in artificial heterostructures through relaxation time modulation. *Science* **2024**, *384*, 312-7. DOI
93. Yang, B.; Liu, Y.; Jiang, R.; et al. Enhanced energy storage in antiferroelectrics via antipolar frustration. *Nature* **2025**, *637*, 1104-10. DOI
94. Xu, R.; Zhu, Q.; Xu, Z.; Feng, Y.; Wei, X. PLZST antiferroelectric ceramics with promising energy storage and discharge performance for high power applications. *J. Am. Ceram. Soc.* **2019**, *103*, 1831-8. DOI
95. Zhang, Y.; Li, Y.; Hao, X.; Jiang, H.; Zhai, J. Flexible antiferroelectric thick film deposited on nickel foils for high energy-storage capacitor. *J. Am. Ceram. Soc.* **2019**, *102*, 6107-14. DOI
96. Wang, X.; Sun, H.; Zhao, H.; et al. Ultrahigh energy storage density and efficiency in orthorhombic PLZST antiferroelectric ceramics via composition regulation. *ACS. Appl. Mater. Interfaces.* **2024**, *16*, 17787-96. DOI

97. Huang, J.; Qi, H.; Gao, Y.; et al. Expanded linear polarization response and excellent energy-storage properties in $(Bi_{0.5}Na_{0.5})TiO_3$-$KNbO_3$ relaxor antiferroelectrics with medium permittivity. *Chem. Eng. J.* **2020**, *398*, 125639. DOI

98. Quan, K.; Zhao, Y.; Meng, X.; et al. High-performance antiferroelectric ceramics via multistage phase transition. *J. Am. Ceram. Soc.* **2022**, *106*, 420-9. DOI

Disclaimer/Publisher's Note: All statements, opinions, and data contained in this publication are solely those of the individual author(s) and contributor(s) and do not necessarily reflect those of OAE and/or the editor(s). OAE and/or the editor(s) disclaim any responsibility for harm to persons or property resulting from the use of any ideas, methods, instructions, or products mentioned in the content.

© The Author(s) 2026. Open Access This article is licensed under a Creative Commons Attribution 4.0 International License (https://creativecommons.org/licenses/by/4.0/), which permits unrestricted use, sharing, adaptation, distribution and reproduction in any medium or format, for any purpose, even commercially, as long as you give appropriate credit to the original author(s) and the source, provide a link to the Creative Commons license, and indicate if changes were made.